Microsc. Microanal. 16, 583–593, 2010
doi:10.1017/S1431927610093761

Microscopy AND Microanalysis

Effects of the Carbon Coating and the Surface Oxide Layer in Electron Probe Microanalysis

Silvina P. Limandri,[1,2] Alejo C. Carreras,[1,2] and Jorge C. Trincavelli[1,2,*]

[1]*Facultad de Matemática, Astronomía y Física, Universidad Nacional de Córdoba, 5000 Córdoba, Argentina*
[2]*Instituto de Física Enrique Gaviola, Consejo Nacional de Investigaciones Científicas y Técnicas de la República Argentina, Córdoba, Argentina*

Abstract: Effects related with the attenuation and deflection suffered by an electron beam when it passes through a carbon conductive coating and an oxide film layer on the surface of bulk samples are studied by Monte Carlo simulations and energy dispersive spectroscopy with electron excitation. Analytical expressions are provided for the primary beam energy and intensity losses and for the deflection of the incident electrons in both layers, in terms of the incidence energy, the film mass thicknesses, and the atomic number of the oxidized element. From these analytical expressions, suitable corrections are proposed for the models used to describe the X-ray spectrum of the substrate, including also the contribution of the X-rays generated in the oxide and conductive films and the characteristic X-ray absorption occurring in those layers. The corrections are implemented in a software program for spectral analysis based on a routine of parameter refinement, and their influence is studied separately in experimental spectra of single-element standards measured at different excitation energies. Estimates for the layer thicknesses are also obtained from the spectral fitting procedure.

Key words: electron probe microanalysis, carbon coating, surface oxidation, modeling of X-ray spectra

Introduction

Image acquisition by scanning electron microscopy (SEM) and chemical characterization by electron probe microanalysis (EPMA) in samples with low electrical conductivity have the inconvenience of charge build up. This effect influences the generation of secondary and backscattered electrons and the excitation of characteristic X-rays. For this reason, it is usual to apply a conductive coating on these types of materials to avoid the charge effect and to reduce the sample heating.

The elements most commonly used for coating in SEM are carbon, gold, silver, platinum, palladium, and chromium. The heavier elements such as gold also have high secondary electron yields, which improve the image quality. Nevertheless, the main disadvantage of gold and silver coatings is their tendency to migrate on the surface of the sample and coalesce into islands or particles that worsen the macroscopic conductivity and mask some fine details of the surface. For high-resolution images, coatings with smaller particle size, e.g., platinum or chromium are used. However, even these elements have a measurable grain size for the highest resolution achievable in SEM (Suzuki, 2002). To improve the resolving power, osmium coatings are used because their grain size is smaller and the thickness required for conductivity is around 1 nm, unlike the several nm necessary for other coating elements.

Carbon is usually the material of choice for microanalysis, due to its excellent transparency and electrical conductivity. Other metal coatings absorb significant amounts of soft X-rays. Effects occurring in the coating film, such as attenuation and deviation of primary electrons, absorption of X-rays emitted by the sample, and generation of photons, are often not taken into account in EPMA because they require knowledge of the conductive film thickness, which is not straightforward. These effects are also produced in the oxide layer spontaneously grown on metallic species. Thus, in a typical analysis of metallic samples, on the material to be analyzed there is an oxide layer upon which the conductive coating is deposited.

Several techniques allow measurement of film thicknesses. They can be classified as destructive, such as cross sections in transmission and scanning electron microscopy and sputter depth profiling (Hoffmann, 1998), and nondestructive, for instance, X-ray photoelectron spectroscopy (XPS) (Alexander et al., 2002), X-ray diffraction (XRD) (Terada et al., 2001), X-ray fluorescence (XRF) (Kolbe et al., 2005), X-ray reflectometry (XRR) (Terada et al., 2001; Thomsen-Schmidt et al., 2004), ellipsometry (Liu et al., 1999), Rutherford backscattering (RBS) (Chu et al., 1978), particle induced X-ray emission (PIXE) (Demortier & Rubalcaba Sil, 1996), quartz crystal microbalance (QCM) (Gold-

Received April 16, 2010; accepted June 1, 2010
*Corresponding author. E-mail: trincavelli@famaf.unc.edu.ar

stein et al., 1994), etc. The main disadvantages associated with the nondestructive techniques listed above are related to availability, lateral resolution, thickness range of application, difficulty in data processing, and need of standards. For instance, RBS requires a particle accelerator and in XPS ultrahigh vacuum is needed; thus, both techniques are not easily available and, in addition, they are not accurate for thicknesses lower than 20 nm and greater than 10 nm, respectively. Another disadvantage of RBS is its limited elemental resolution for small relative atomic number differences. On the other hand, XRD works properly only for thicknesses greater than 100 nm; the methods involving XRF and PIXE are based on calibration curves, which must be performed for each particular configuration. Regarding XRR and ellipsometry, these techniques have a limited lateral resolution, particularly around a few mm for the latter, which also requires a complicated data treatment. Finally, QCM must be previously calibrated using another technique in order to perform an absolute thickness determination (Bastin & Heijligers, 2000*b*; Campos et al., 2002).

X-ray spectra measured in EPMA can be used to determine layer thicknesses in the nanometric range, relevant for the oxidation layer and the conductive coating usually found in materials characterization. For instance, calibration curves were performed by measuring spectra of particular films (Bastin & Heijligers, 2000*a*, 2000*b*) or substrates (Campos et al., 2001, 2002). Additional efforts were done to achieve a general method capable of determining the film thickness in a film/substrate system with arbitrary composition (Kyser & Murata, 1974; Yakowitz & Newbury, 1976; Bastin & Heijligers, 2000*a*). Moreover, some commercial software packages, such as X-FILM (Merlet, 1995), MLA (Bastin et al., 1998), STRATAGem (Pouchou & Pichoir, 1990), and LAYERF (Pouchou & Pichoir, 1990), allow determination of the film thicknesses and compositions in more complex configurations of stratified samples. Each of these software programs assumes a particular model for the ionization depth distribution function $\varphi(\rho z)$ in a bulk specimen. These approaches, broadly, are based on the construction of a function $\varphi(\rho z)$ on the basis of fictitious homogeneous samples. From the integration of this expression for $\varphi(\rho z)$ along the mass thickness traveled by the electrons in each layer and the experimental peak intensities, layer compositions and thicknesses are obtained through a complicated iterative process. The method becomes more difficult when the same element is present in a film and in the substrate or in more than one layer.

In the present work, the effects produced by a carbon coating and an oxide layer on a bulk metallic substrate were studied, and their influence in the modeling of spectra was analyzed separately. The attenuation and deflection of the incident electron beam in both layers were studied by Monte Carlo simulation. Analytical expressions are provided for the energy and intensity losses of the primary beam and for the deflection of the incident electrons in a carbon coating film and in an oxide layer grown on a metallic substrate. From these analytical expressions, suitable corrections were introduced in a model that predicts the X-ray spectrum emitted by a sample, including also the contribution of the X-rays generated in the oxide and conductive films and the characteristic X-ray absorption occurring in those layers. The corrections obtained here were implemented in software for spectral analysis based on a routine of parameter refinement (Bonetto et al., 2001), which is intended to determine both layer mass thicknesses and the substrate composition, provided that certain parameters are well known (see the Prediction of Spectra subsection). The corrections proposed were tested in experimental spectra of single-element standards measured at several incident energies.

If the effects of both layers on experimental spectra are ignored, quantitative analysis could not be reliably performed in some cases, such as low incidence energy, thick carbon, or oxide layers, or analysis using soft characteristic X-rays. In these cases, important errors could be introduced in standardless and conventional analyses when the unknown and standards are not identically coated or oxidized.

Methods and Materials

Simulations and Measurements

Effects produced by the carbon conductive coating and the native oxide layer were studied by means of Monte Carlo simulations. To this purpose, the software package PENELOPE, developed by Salvat et al. (2003), was used to simulate an electron beam impinging perpendicularly on a specimen composed by a carbon layer deposited on an oxide film. Different incidence energies E_o (3, 6, 9, 12, 15, 18, 21, and 27 keV), carbon thicknesses z_C (5, 10, 30, 60, and 100 nm), and oxide thicknesses z_{Ox} (5, 10, 20, 50, 80, and 150 nm) were simulated for oxides of several elements (Mg, Si, Sc, Cr, Ni, and Zn). For the thickest layers tested and when simulations for $E_o = 3$ keV resulted in very few transmitted electrons, additional simulations were carried out for $E_o = 3.5$, 4, 4.5, 5, and 5.5 keV. The assumed mass densities were 2, 3.6, 2.533, 3.86, 5.2, 6.7, and 5.6 g/cm^3 for C, MgO, SiO_2, Sc_2O_3, Cr_2O_3, NiO, and ZnO, respectively. All of the calculations amounted to more than 1,600 runs in approximately 300 h of simulation, each of which comprises several millions of electron trajectories.

Si and Mg X-ray spectra were measured using SPI #02751 standards to test the results obtained by Monte Carlo simulations. Measurements were performed with a LEO 1450VP scanning electron microscope from the Laboratorio de Microscopía Electrónica y Microanálisis (LABMEM) of the Universidad Nacional de San Luis, Argentina. This equipment is furnished with an EDAX Genesis 2000 energy dispersive spectrometer with a resolution of 129 eV for the Mn-Kα line (5.893 keV). The detector is a Si(Li) SUTW Sapphire with ultrathin polymer window Moxtek

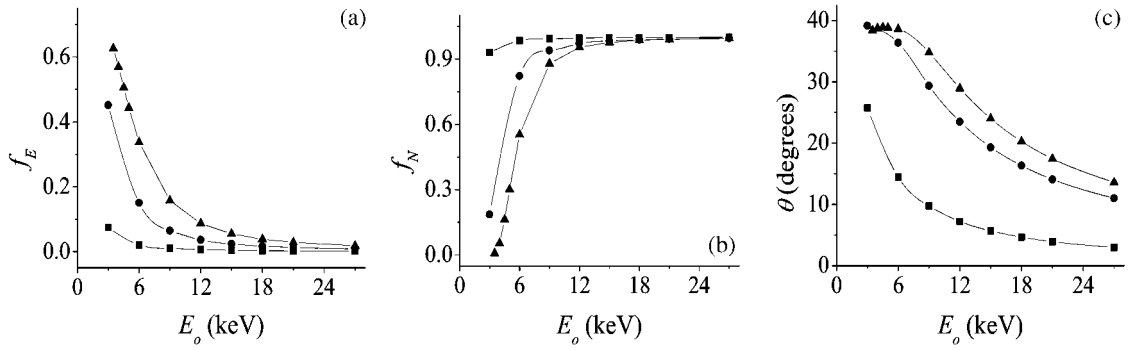

Figure 1. Parameters f_E, f_N, and θ resulting from the Monte Carlo simulations as functions of E_o for a 10 nm thick carbon coating on MgO (triangles), Cr_2O_3 (circles), and ZnO (squares) films. The oxide thicknesses shown are 150 nm for MgO, 50 nm for Cr_2O_3, and 5 nm for ZnO. The uncertainty bars are below the symbol size in all the cases.

AP3.3 containing a 380 μm thick silicon support structure with 77% open area and aluminum ohmic contact. The spectra were measured at E_o = 3, 6, 9, 12, 15, and 18 keV, with a beam current ranging between 1.1 and 1.7 nA during a live acquisition time of 100 s for each spectrum.

Results and Discussion

From the point of view of matrix corrections in quantitative EPMA, four major effects are caused by the coating and oxide films: attenuation of the electron beam current, attenuation of the electron energy, deflection of the electron beam, and X-ray attenuation. These effects were studied separately by Kato (2007) and by Osada (2005), but only in a few samples.

To study the first three effects, three parameters were considered: the fraction of energy lost by the incident electrons f_E, the fraction of transmitted electrons f_N, and the average deflection angle θ with respect to the incidence direction. The fourth effect is directly related to both layer thicknesses. The behavior of the parameters considered was investigated as a function of E_o, the total mass thickness $\rho z = \rho_C z_C + \rho_{Ox} z_{Ox}$, and the sum of the mass thicknesses weighted by the atomic numbers $S = \rho_C Z_C z_C + \rho_{Ox} Z_{el} z_{Ox}$, where ρ_i and Z_i are the density and the atomic number of the material i, respectively; particularly Z_{el} corresponds to the oxidized element and the subindexes C and Ox correspond to the carbon and oxide layers, respectively.

The data processing was carried out in different stages. First, the dependence of the three parameters on the incidence energy was studied for each particular oxide and each carbon and oxide thickness, and a set of fitting coefficients was determined. The behavior of f_E, f_N, and θ as a function of E_o is exemplified in Figure 1 for MgO, Cr_2O_3, and ZnO with thicknesses z_C = 10 nm and z_{Ox} = 150, 50, and 5 nm, respectively. In a second step, the coefficients obtained in the first one were, in turn, parameterized in terms of ρz and S.

The functions obtained for the three parameters are described as follows. All of them must be assessed with energies in keV, mass densities in g/cm^3, thicknesses in cm, and angular deflections in degrees.

Fraction of Energy Lost by the Incident Electrons

Some preliminary considerations are helpful to find an adequate fitting function for the parameter f_E. The average energy dE loss by an electron of kinetic energy E while traveling through a small path of length ds within a material medium is characterized by the stopping power, which can be expressed by the semiclassical approximation given by Bethe (1930) and modified by Joy and Luo (1989) to properly describe the low energy behavior

$$\frac{dE}{ds} = -7.85 \times 10^{-2} \frac{Z\rho}{AE} \ln\left(\frac{1.166E}{J^*}\right), \qquad (1)$$

with

$$J^* = \frac{J}{1 + k/E},$$

where $J \cong 0.0115 \times Z$ keV is the mean ionization potential of the atom, $k = 0.731 + 0.0688 \log_{10} Z$, and A is the atomic weight. As can be seen from equation (1), the dependence of the stopping power on Z is very weak because Z/A is practically constant and the dependence through J is smoothed by the logarithm function. Hence, equation (1) can be approximated by

$$\frac{dE}{ds} = const \times \frac{\rho}{E}.$$

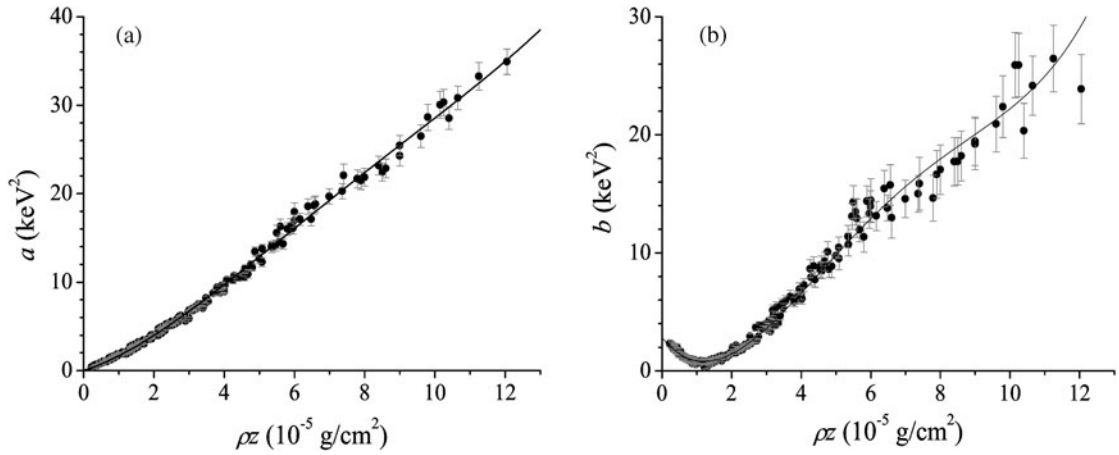

Figure 2. Coefficients a and b for the parameter f_E. The dots represent values obtained from each simulation with the fitting function proposed in equation (3); the uncertainty bars correspond to one standard deviation. The solid line is the parameterization given in (**a**) equation (4) and (**b**) equation (5).

Then, the fractional energy loss while crossing a thin layer of thickness z is basically given by

$$\frac{\Delta E}{E} = const \times \frac{\rho z}{E^2}. \tag{2}$$

Bearing in mind the functional behavior expected, shown in equation (2), the expression proposed to fit the simulated data for f_E is

$$f_E = \frac{a}{b + E_o^2}. \tag{3}$$

It is important to emphasize that in spite of the simplicity of the fitting function given in equation (3), the fitted data contain all the physics considered in the realistic Monte Carlo package used (Salvat et al., 2003).

Values were obtained for the coefficients a and b for each mass thickness; they are plotted in Figure 2 along with the respective parameterization functions whose expressions are

$$a = a_1\rho z + a_2(\rho z)^2 + a_3(\rho z)^3 + a_4(\rho z)^4 \tag{4}$$

and

$$b = b_0 + b_1\rho z + b_2(\rho z)^2 + b_3(\rho z)^3 + b_4(\rho z)^4. \tag{5}$$

The coefficients a_i and b_i of these functions are given in Table 1. The function found for f_E [equation (3)] depends only on the mass thickness and the incidence energy as the expression derived from the stopping power formula [equation (2)]. Moreover, as can be seen from Figure 2a, the coefficient a is roughly linear with respect to ρz, showing the same behavior as the numerator of equation (2). In addition, the denominators of equations (2) and (3) present a similar trend with the electron energy because it can be seen that the coefficient b is much smaller than E_o^2 for all the cases where f_N is not negligible.

The differences between the expression for f_E given by equation (3) and the corresponding simulated data are lower than 0.02 for 91% of the cases, while they are between 0.02 and 0.05 for 7% of the values; the remaining 2%

Table 1. Coefficients for the Parameters f_E, f_N, and θ, Corresponding to Equations (4), (5), (7), (8), (11), (12), and (13).

Coefficient	$i = 0$	$i = 1$	$i = 2$	$i = 3$	$i = 4$
a_i		$1.2874\cdot10^{5}$	$4.244\cdot10^{9}$	$-4.035\cdot10^{13}$	$1.3584\cdot10^{17}$
b_i	2.8114	$-3.5736\cdot10^{5}$	$1.8168\cdot10^{10}$	$-2.0223\cdot10^{14}$	$7.5682\cdot10^{17}$
c_i		$1.905\cdot10^{-2}$	0.41		
d_i		2.226	1.188	0.36719	
m_i	0.8192	$-6.3419\cdot10^{2}$	$3.0414\cdot10^{5}$	$-5.446\cdot10^{7}$	
n_i	0.1766	$-1.2325\cdot10^{2}$	$1.3484\cdot10^{5}$	$-5.72\cdot10^{7}$	$8.8025\cdot10^{9}$
p_i	0.2878	$5.7188\cdot10^{4}$	$-6.429\cdot10^{8}$	$3.6016\cdot10^{12}$	

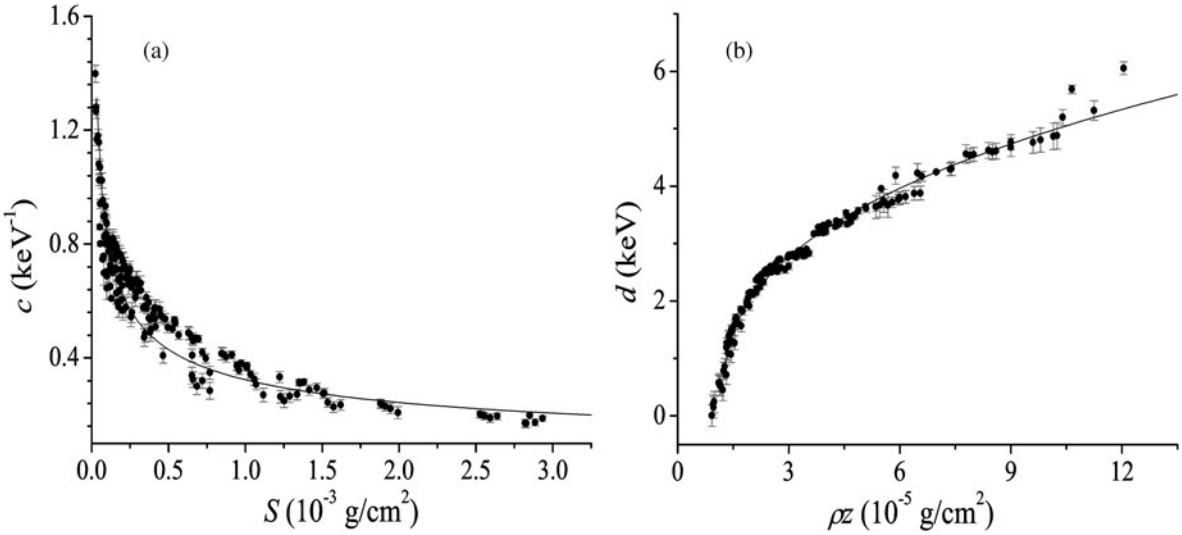

Figure 3. Coefficients c and d for the parameter f_N. The dots represent values obtained from each simulation with the fitting function proposed in equation (6); the uncertainty bars correspond to one standard deviation. The solid line is the parameterization given in (**a**) equation (7) and (**b**) equation (8).

corresponds to data predicted with differences higher than 0.05. It is worth emphasizing that the differences between the values assessed by equation (3) and the simulated ones do not present any appreciable trend with the mass thickness, although the prediction is slightly worse for low incidence energies.

Fraction of Transmitted Electrons

The expression found for the fraction of transmitted electrons is given by the attenuation law

$$f_N = \max\begin{cases} 1 - e^{-c(E_o - d)} \\ 0 \end{cases}. \tag{6}$$

The coefficients c and d obtained for each S and ρz, respectively, are shown in Figure 3 together with their fitting functions, which are given by

$$c = c_1 S^{-c_2} \tag{7}$$

and

$$d = d_1(\rho z \cdot 10^5 - d_2)^{d_3}. \tag{8}$$

In equation (8), the expression within the parentheses must be positive or zero; otherwise it must be replaced by zero. The coefficients c_i and d_i are given in Table 1. From equation (6) and the expressions for the parameters c and d [equations (7) and (8)], it can be observed that the transmitted fraction depends not only on E_o and ρz, but also on S.

The fraction of transmitted electrons is related to the combined effects of both inelastic and elastic processes; therefore, one expects to find a dependence on E_o and ρz as well as on Z, due to the dependence of the elastic nuclear cross section σ for dispersion angles greater than φ on the atomic number. According to Evans (1955),

$$\sigma(>\varphi) = 1.62 \times 10^{-20} \frac{Z^2}{E^2} \cot^2\left(\frac{\varphi}{2}\right) \text{cm}^2/\text{atom}. \tag{9}$$

Similar to the parameter f_E, the largest discrepancies are found for the lowest energies, although the differences between the model for f_N and the simulated electron transmission do not present any appreciable trend with the variables ρz and S. The differences between the expression given for f_N [equation (6)] and the simulated data are below 0.02 for 75% of the cases, while they are between 0.02 and 0.05 for 14% of the values, and the remaining 11% corresponds to data predicted with differences higher than 0.05.

Average Deflection Angle

An analytical function was fitted to the results of the deflection angle obtained from the simulations paying special attention to intermediate and large mass thicknesses, where the deviation introduces appreciable effects in the generation and attenuation of characteristic X-rays. The function obtained is

$$\theta = 39.3° \frac{1 - m\tanh(nE_o - p)}{1 - m\tanh(-p)}. \tag{10}$$

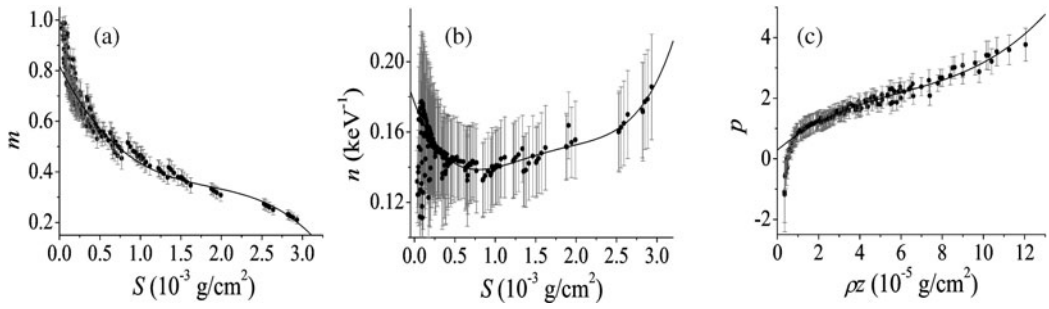

Figure 4. Coefficients m, n, and p for the parameter θ. The dots represent values obtained from each simulation with the fitting function proposed in equation (10); the uncertainty bars correspond to one standard deviation. The solid line is the parameterization given in (**a**) equation (11), (**b**) equation (12), and (**c**) equation (13).

The coefficients m and n for each S value, and p for each mass thickness are plotted in Figure 4 along with the respective parameterization functions whose expressions are given by

$$m = m_0 + m_1 S + m_2 S^2 + m_3 S^3, \tag{11}$$

$$n = n_0 + n_1 S + n_2 S^2 + n_3 S^3 + n_4 S^4, \tag{12}$$

and

$$p = p_0 + p_1 \rho z + p_2 (\rho z)^2 + p_3 (\rho z)^3. \tag{13}$$

The coefficients m_i, n_i, and p_i are given in Table 1. The deflection angle is mainly determined by the elastic interactions [see equation (9)]. For this reason, the θ dependence on E_o, ρz, and S is expected. For large thicknesses or low incidence energies, equation (10) tends to the finite value 39.3°. The existence of this upper limit can be understood taking into account that the mean deflection angle θ of the transmitted electrons can be expressed as

$$\theta = \frac{\int_0^{\pi/2} 2\pi n_\phi \phi \sin\phi \, d\phi}{\int_0^{\pi/2} 2\pi n_\phi \sin\phi \, d\phi}, \tag{14}$$

where n_ϕ is the number of electrons transmitted with an angle between ϕ and $\phi + d\phi$. In the case of isotropic deflections, n_ϕ is a constant, and equation (14) gives the value $\theta = 1$ rad (i.e., 57°). However, as the isotropization begins above the bottom surface, lower deflection angles are favored because the electrons dispersed at larger angles must travel a greater distance inside the layer, before reaching the bottom surface. For this reason, the mean deviation angle θ resulting from the simulations is lower than the one corresponding to the isotropic case.

As can be seen from Figure 4, the parameters n and p are poorly predicted by the proposed fitting functions for low S and ρz values, respectively. Nevertheless, these cases correspond to thin layers, where the influence of θ in the modeling of the X-ray spectrum is not important. Moreover, the corrections related to this parameter are less important than the ones associated to f_N and f_E as will be discussed below. For the whole dataset, the differences between the expression for θ given by equation (10) and the simulated results are lower than 2° for 78% of the cases, while they are between 2° and 4° for 19% of the values; the remaining 3% corresponds to data predicted with differences higher than 4°.

The overall behavior of f_E, f_N, and θ is shown in Figures 5a, 5b, and 5c, respectively. Figure 5a involves all the studied materials, while Figures 5b and 5c correspond to a 20 nm carbon coating on NiO films of different thicknesses, although its behavior is similar to that of the remaining oxides. It can be seen that the transmitted energy fraction $(1 - f_E)$ and the fraction of transmitted electrons f_N decrease with the layer thickness and increase with E_o, as expected. On the other hand, the deflection angle increases with the film thickness, reaching a saturation value as explained above, whereas it decreases with E_o.

Influence of the Parameters Studied on the X-Ray Spectra

The effects of the parameters f_E, f_N, and θ due to the presence of the oxide and conductive carbon layers on experimental X-ray spectra from single-element specimens were analyzed by using software for spectral processing in EPMA, based on a parameter optimization method (Bonetto et al., 2001; Limandri et al., 2008). This method consists of minimizing the differences between the experimental spectrum and an analytical function proposed to describe it. This function takes into account characteristic peaks, bremsstrahlung, and different detection artifacts. The detected characteristic intensity $P_{s,q}$ of the line q from element s in the sample without neither oxidation film nor conductive coating is given according to Trincavelli and Van Grieken (1994)

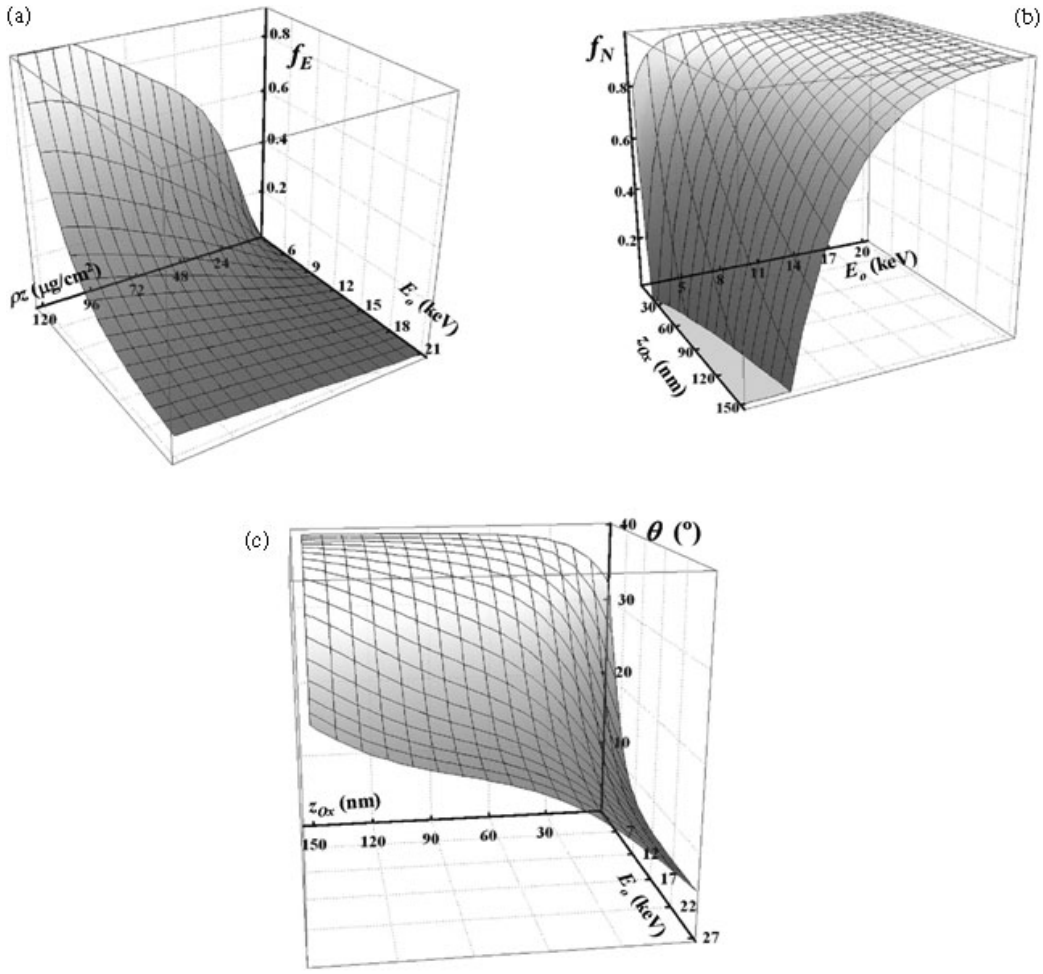

Figure 5. Three-dimensional representation of the parameters studied. (**a**) f_E as a function of the total mass thickness and E_o, (**b**) f_N, and (**c**) θ, as functions of the oxide thickness and E_o. Panels **b** and **c** correspond to a 20 nm carbon film on NiO layers of different thicknesses.

$$P_{s,q} = C_s(\boldsymbol{ZAF})_{s,q} Q_s \omega_s f_{s,q} \varepsilon(E_{s,q}) \frac{\Delta\Omega}{4\pi} it, \qquad (15)$$

where $\boldsymbol{Z}$, $\boldsymbol{A}$, and $\boldsymbol{F}$ indicate the atomic number, absorption, and fluorescence matrix corrections, respectively; Q_s is the ionization cross section for the involved atomic shell of element s at the incident electron energy E_o; ω_s is the fluorescence yield for the considered atomic shell; $f_{s,q}$ is the relative transition probability of the observed line q; $\varepsilon(E_{s,q})$ is the detector intrinsic efficiency evaluated at the characteristic energy of the line q; $\Delta\Omega$ is the solid angle subtended by the detector; i is the beam current; and t is the live acquisition time. The $\boldsymbol{ZA}$ combined correction depends on the sample concentrations C_s in a complicated way, which may be obtained from the ionization distribution function $\varphi(\rho z)$ with mass depth ρz. As proposed by Packwood and Brown (1981), this function can be written as

$$\varphi(\rho z) = \exp[-\alpha^2(\rho z)^2]\{\gamma - (\gamma - \varphi_o)\exp[-\beta(\rho z)]\}.$$

Let us now consider a single-element metallic sample with a surface oxidation layer of thickness z_{Ox} and a carbon coating of thickness z_C. These films emit X-rays and attenuate the X-rays coming from the substrate. Their influence on the detected intensity is described as follows.

The effective incidence energy influences the ionization cross section and the surface ionization involved in the oxide layer. These parameters are mainly responsible for the characteristic X-ray emission from oxygen and the oxidized element in this foil.

Regarding the production of characteristic X-rays in the substrate, the loss of a fraction of the incidence energy in the surface layers directly affects the effective overvoltage, which in turn influences the parameters involved in the $\varphi(\rho z)$ function and the ionization cross section. In addition, the bremsstrahlung emission from the substrate also depends on the effective incidence energy.

The fact that only a fraction of the incident electrons reaches the oxide layer and the substrate implies a diminu-

tion of the effective incidence current, which is proportional to the intensity of the X-rays emitted by the oxide film and the substrate, respectively. On the other hand, the decrease in the number of electrons reaching the substrate modifies the surface ionization in the oxide layer, which affects the X-ray emission of this film.

Due to the departure from the incident direction, the η coefficient of the sample increases, with a corresponding increase in the function $\varphi(\rho z)$ and thus in the intensity of the characteristic X-ray emission.

The incidence on the oxide layer is also nonnormal due to the deflection in the carbon layer. This deviation causes two effects: an increase in the effective thickness of this layer and, on the other hand, an increment in the number of electrons backscattered from it, which in turn produces an enhancement of the oxide film surface ionization φ_o. Both effects contribute to a greater generation of O-Kα characteristic photons, as well as to an increase in the characteristic X-rays produced by the metal forming the oxide.

Prediction of Spectra

Corrections introduced by the parameters f_E, f_N, θ, and by the X-ray generation and attenuation in both layers were tested in Si and Mg spectra from pure standards, spontaneously oxidized and coated with a carbon conductive layer, measured at different excitation energies. To this purpose, the analytical expressions obtained for the corrections were implemented in the software based on the parameter optimization method mentioned above. Figure 6 shows an example of the influence of these layers in a Mg spectrum measured at $E_o = 15$ keV, whereas Figure 7 exemplifies the same kind of effects for Si measured at $E_o = 3$ keV. In Figures 6a, 7a, the layers are completely ignored; as can be seen, the C-Kα and O-Kα peaks are not predicted; in addition, the characteristic peak produced in the substrate is overestimated mainly because the attenuation in the surface layers is disregarded. The improvement achieved when the attenuation and the contribution of the X-ray generation taking place in both films is considered can be seen in Figures 6b, 7b. Nevertheless, the prediction is still incomplete because the effects introduced by the parameters f_E, f_N, and θ are not taken into account. Finally, when the full correction given by equations (3), (6), and (10) is considered (Figs. 6c, 7c), a good description is achieved. The goodness of fit is assessed by the parameter χ^2 defined by

$$\chi^2 = \frac{1}{N - N_P} \sum_i \frac{(I_i^{exp} - I_i)^2}{I_i^{exp}},$$

where N is the number of spectral channels, N_P is the number of parameters to optimize, I_i is the predicted intensity corresponding to the channel i, and I_i^{exp} refers to the experimental spectrum; the sum runs over all the channels in the fitted region. As can be seen in Figures 6, 7, the decrease in χ^2 indicates an improvement of the spectral description when more corrections are introduced.

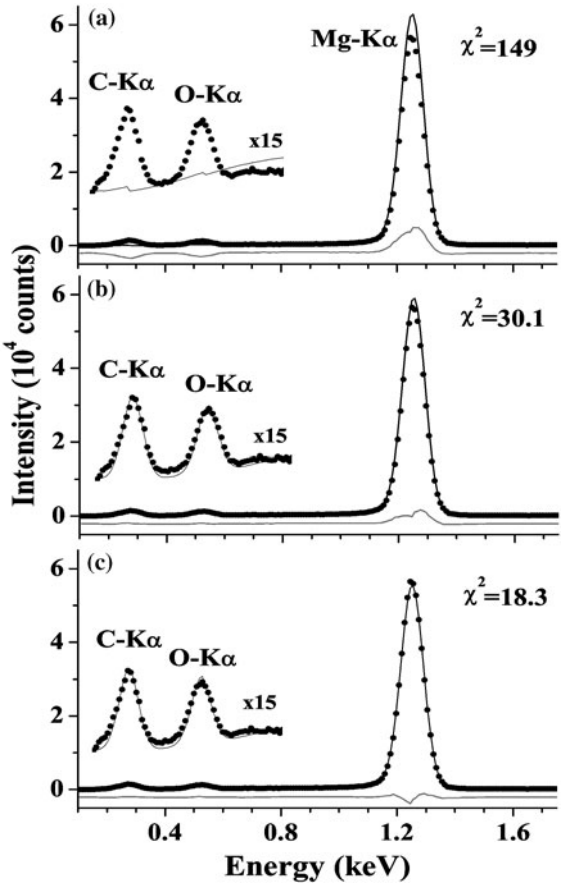

Figure 6. Example of different stages in the prediction of a Mg spectrum measured at $E_o = 15$ keV, related to the presence of oxide and carbon layers. Dots, experimental; black line, prediction; gray line, differences between experimental and calculated data. **a:** No layers were considered. **b:** Spectrum predicted only taking into account the X-ray generation and the attenuation in both layers. **c:** X-ray generation and attenuation in both layers; and the parameters f_E, f_N, and θ were considered.

The intensity predicted for the carbon Kα peak is proportional to z_C, to the detector efficiency ε at the characteristic C-Kα energy, and to other atomic and experimental parameters independent of the photon energy. If accurate thickness determinations are searched, the detector efficiency and the remaining parameters must be well known. The model used to calculate the efficiency curve depends on the characteristic thicknesses of the detector, as explained by Trincavelli et al. (2008). Typically, the efficiency is poorly known at low energies because the mass absorption coefficients at this energy range and the detector parameters are not very well known; however, the product $\varepsilon \cdot z_C$, required to describe the spectrum and eventually to carry out standardless quantification, can be obtained from the minimization procedure even if the detector efficiency is not well

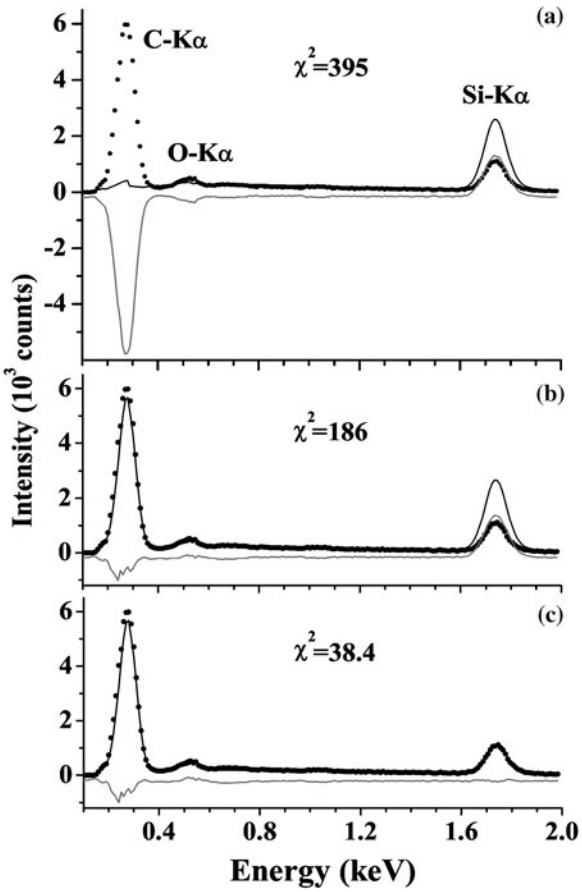

Figure 7. Example of different stages in the prediction of a Si spectrum measured at $E_o = 3$ keV, related to the presence of oxide and carbon layers. Dots, experimental; black line, prediction; gray line, differences between experimental and calculated data. **a:** No layers were considered. **b:** Spectrum predicted only taking into account the X-ray generation and the attenuation in both layers. **c:** X-ray generation and attenuation in both layers; and the parameters f_E, f_N, and θ were considered.

known. A similar reasoning can be applied to the O-Kα peak and the z_{Ox} thickness.

For each spectrum, measured for Mg and Si at several incidence energies, carbon and oxide film thicknesses were estimated from the optimization procedure. The average thicknesses obtained are $z_C = 53.1 \pm 1.3$ nm and 34 ± 4 nm, and $z_{Ox} = 97 \pm 4$ nm and 8 ± 2 nm for Mg and Si standards, respectively. It must be taken into account that the thicknesses obtained are actually mass thicknesses; the presented values for z_C and z_{Ox} depend on the mass densities assumed, which are given in the Simulations and Measurements subsection. The relative uncertainty in the estimation of the SiO_2 layer thickness is large because its main indicator, given by the O-Kα peak intensity, is very low in this case. Bearing this fact in mind, it can be inferred that the lower limit for thickness estimation by this method is a few nanometers.

It can be seen from Figures 6, 7 that the influence of the surface layers is more important in the Si spectrum, due to the low incident energy used for the measurement, although the SiO_2 layer is much thinner than the MgO foil. In fact, the values obtained from equations (3), (6), and (10) are $f_E = 0.05$ and 0.14; $f_N = 0.99$ and 0.94; $\theta = 21°$ and 31°, for Mg and Si, respectively; i.e., the effects are most important for Si. In addition, the coarse underestimation in the description of the C-Kα region of the Si spectrum without performing corrections (see Fig. 7a) is expected because the low excitation energy is very effective for the ionization of carbon atoms.

On the other hand, it must be borne in mind that an error in the value of the effective incidence energy may produce important deviations in the assessment of the ionization cross sections Q. In the case illustrated by Figure 7, for instance, the value for Q_{Si} is underestimated at 33.5% when the incidence energy is taken as the nominal value instead of the effective value after the beam is transmitted through both films.

The corrections introduced by the different parameters can be observed with more detail in Figure 8, which corresponds to a spectrum obtained from the Mg standard measured at $E_o = 6$ keV. As in the previous examples, the C-Kα and O-Kα characteristic peaks reveal the presence of the carbon and oxide films. As can be seen from Figure 8a, if these layers are ignored, the spectrum cannot be adequately described. The prediction of the spectrum also considers the Fe-L spurious radiation coming from the specimen chamber, as can be observed around 0.7 keV. This small peak is largely overestimated because the X-ray attenuation in both surface layers is not taken into account in this first stage. The generation of characteristic X-rays in both films and the attenuation of the radiation coming from the substrate in those layers are considered in Figure 8b. As can be observed, even when both C-Kα and O-Kα peaks are properly described, the Mg characteristic peak is overestimated. In Figure 8c, the effective incidence energy is considered by introducing the parameter f_E and a reasonable fitting is achieved. The prediction improves when the actual number of transmitted electrons is introduced (Fig. 8d) through the parameter f_N. Finally, in Figure 8e all the corrections are performed and the best fit is achieved. The importance of the effects studied decreases from Figures 8a to 8e, as can be observed from the corresponding χ^2 values. In this particular case, the most influential parameter is f_E, the second one is f_N, and the weakest one is θ; nevertheless, the order of importance of the corrections could be different in other cases.

Conclusions

The influence of several effects associated with the presence of a carbon coating and an oxide layer on metal substrates

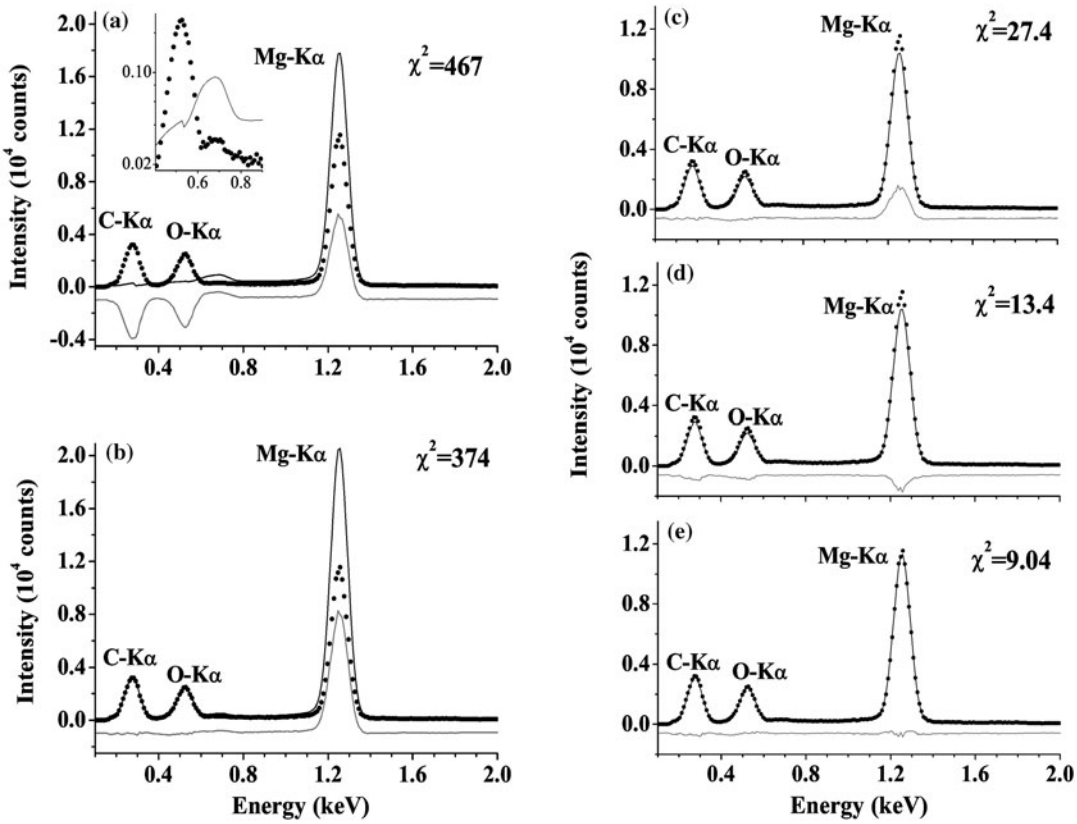

Figure 8. Example of different stages in the prediction of a Mg spectrum measured at $E_o = 6$ keV, related to the presence of oxide and carbon layers. Dots, experimental; black line, prediction; gray line, differences between experimental and calculated data. **a:** No layers were considered. Inset: Detailed O-Kα region in logarithmic scale. **b:** Spectrum predicted only taking into account the X-ray generation and the attenuation in both layers. **c:** The f_E parameter is also considered. **d:** f_N is also taken into account. **e:** The full correction procedure is carried out (the X-ray generation and the attenuation in both layers, and the parameters f_E, f_N, and θ are considered).

was studied separately for EPMA. The fraction of energy lost by the incident electrons in the surface layers, the fraction of transmitted electrons, and the average deflection angle were evaluated with Monte Carlo simulations. From the simulated data, analytical expressions were obtained for the three parameters mentioned as functions of the incident beam energy, the mass thicknesses, and the atomic numbers involved. These expressions were implemented in a software program for thickness determination and quantitative analysis. The presence of the layers affects the modeling of spectra through different processes involving the generation and attenuation of characteristic X-rays and bremsstrahlung in the substrate as well as in the surface layers.

The spectral modeling was tested with experimental spectra of Mg and Si standards coated with a carbon layer and spontaneously oxidized, which were measured at several excitation energies. The spectra were properly fitted when all the effects studied here were considered.

The thicknesses of both layers were determined by assuming certain models for the factors appearing in equation (15). However, some of them are not well known for low energies, particularly the detection efficiency. For this reason, a careful characterization of the detector in this energy range in order to get absolute thicknesses with low uncertainties would be necessary. Nevertheless, with this approach, a very good spectral description was achieved, which is necessary for reliable quantitative analysis.

Additional research should be done to include the effect of bremsstrahlung generated within the surface layers as well as to extend the present study to other materials typically used as conductive coatings in EPMA.

Finally, it must be remarked that the oxide and conductive layers also affect the emission of backscattered electrons from the substrate. For this reason, it would be of interest to investigate their influence on the chemical contrast images that can be obtained from these types of electrons.

Acknowledgments

This work was partially supported by the Consejo Nacional de Investigaciones Científicas y Técnicas of the Argentine

Republic and the Secretaría de Ciencia y Técnica of the Universidad Nacional de Córdoba, Argentina.

References

Alexander, M.R., Thompson, G.E., Zhou, X., Beamson, G. & Fairley, N. (2002). Quantification of oxide film thickness at the surface of aluminium using XPS. *Surf Interface Anal* **34**, 485–489.

Bastin, G.F., Dijkstra, J.M., Heijligers, H.J.M. & Klepper, D. (1998). In-depth profiling with the electron probe microanalyzer. In *Proceedings EMAS'98 3rd Regional Workshop*, Llovet, X., Merlet, C. & Salvat, F. (Eds.), pp. 25–55. Barcelona: Universitat de Barcelona.

Bastin, G.F. & Heijligers, H.J.M. (2000*a*). A systematic database of thin-film measurements by EPMA part I—Aluminum films. *X-Ray Spectrom* **29**, 212–238.

Bastin, G.F. & Heijligers, H.J.M. (2000*b*). A systematic database of thin-film measurements by EPMA part II—Palladium films. *X-Ray Spectrom* **29**, 373–397.

Bethe, H.A. (1930). Zur Theorie des Durchgangs schneller Korpuskularstrahlen durch Materie. *Ann Phys* **397**, 325–400.

Bonetto, R., Castellano, G. & Trincavelli, J. (2001). Optimization of parameters in electron probe microanalysis. *X-Ray Spectrom* **30**, 313–319.

Campos, C.S., Coleoni, E.A., Trincavelli, J.C., Kaschny, J., Hubbler, J., Soares, M.R.F. & Vasconcellos, M.A.Z. (2001). Metallic thin film thickness determination using electron probe microanalysis. *X-Ray Spectrom* **30**, 253–259.

Campos, C.S., Vasconcellos, M.A.Z., Llovet, X. & Salvat, F. (2002). Measurements of L-shell X-ray production cross sections of W, Pt, and Au by 10–30-keV electrons. *Phys Rev A* **66**, 012719.

Chu, W., Meyer, J. & Nicolet, M. (1978). *Backscattering Spectrometry*. New York: Academic Press.

Demortier, G. & Rubalcaba Sil, J.L. (1996). Differential PIXE analysis of Mesoamerican jewelry items. *J Nucl Instrum Meth Phys Res B* **118**, 352–358.

Evans, R.D. (1955). *The Atomic Nucleus*. New York: McGraw-Hill.

Goldstein, J.I., Newbury, D.E., Echlin, P., Joy, D.C., Romig, A.D., Jr., Lyman, C.E., Fiori, C. & Lifshin, E. (1994). *Scanning Electron Microscopy and X-Ray Microanalysis*, 2nd ed. New York: Plenum Press.

Hoffmann, S. (1998). Sputter depth profile analysis of interfaces. *Rep Prog Phys* **61**, 827–888.

Joy, D.C. & Luo, S. (1989). An empirical stopping power relationship for low-energy electrons. *Scanning* **11**, 176–180.

Kato, T. (2007). Monte Carlo study of quantitative electron probe microanalysis of monazite with a coating film: Comparison of 25 nm carbon and 10 nm gold at $E_0 = 15$ and 25 keV. *Geostand Geoanal Res* **31**, 89–94.

Kolbe, M., Beckhoff, B., Krumrey, M. & Ulm, G. (2005). Thickness determination for Cu and Ni nanolayers: Comparison of completely reference-free fundamental parameter-based X-ray fluorescence analysis and X-ray reflectometry. *Spectrochim Acta B* **60**, 505–510.

Kyser, D.F. & Murata, K. (1974). Quantitative electron microprobe analysis of thin films on substrates. *IBM J Res Dev* **18**, 352–363.

Limandri, S., Trincavelli, J., Bonetto, R. & Carreras, A. (2008). Structure of the Pb, Bi, Th and U M X-ray spectra. *Phys Rev A* **78**, 022518.

Liu, C., Erdmann, J. & Macrander, A. (1999). *In situ* spectroscopic ellipsometry as a surface-sensitive tool to probe thin film growth. *Thin Solid Films* **355**, 41–48.

Merlet, C. (1995). A new quantitative procedure for stratified samples in EPMA. In *Proceedings 29th Annual Conference of the Microbeam Analysis Society*, Etz, E.S. (Ed.), p. 203. New York: VHC Publishers.

Osada, Y. (2005). Monte Carlo study of quantitative EPMA analysis of a nonconducting sample with a coating film. *X-Ray Spectrom* **34**, 96–100.

Packwood, R. & Brown, J. (1981). A Gaussian expression to describe $\varphi(\rho z)$ curves for quantitative electron probe microanalysis. *X-Ray Spectrom* **10**, 138–146.

Pouchou, J.L. & Pichoir, F. (1990). Surface film X-ray microanalysis. *Scanning* **12**, 212–224.

Salvat, F., Fernández-Varea, J. & Sempau, J. (2003). PENELOPE—A code system for Monte Carlo simulation of electron and photon transport. Issy-les-Molineaux, France: OECD/NEA Data Bank.

Suzuki, E. (2002). High-resolution scanning electron microscopy of immunogold-labelled cells by the use of thin plasma coating of osmium. *J Microsc* **208**, 153–157.

Terada, S., Murakami, H. & Nishihagi, K. (2001). Thickness and density measurement for new materials with combined X-ray technique. SEMICON Europa 2001, Munich, April 23.

Thomsen-Schmidt, P., Hasche, K., Ulm, G., Herrmann, K., Krumrey, M., Ade, G., Stümpel, J., Busch, I., Schädlich, S., Schindler, A., Frank, W., Hirsch, D., Procop, M. & Beck, U. (2004). Realisation and metrological characterisation of thickness standards below 100 nm. *Appl Phys A* **78**, 645–649.

Trincavelli, J., Limandri, S., Carreras, A. & Bonetto, R. (2008). Experimental method to determine the absolute efficiency curve of a wavelength dispersive spectrometer. *Microsc Microanal* **14**, 306–314.

Trincavelli, J. & Van Grieken, R. (1994). Peak-to-background method for standardless electron microprobe analysis of particles. *X-Ray Spectrom* **23**, 254–260.

Yakowitz, H. & Newbury, D.E. (1976). A simple analytical method for thin film analysis with massive pure element standards. In *Proceedings 9th Annual Scanning Electron Microscope Symposium*, vol. 1, pp. 151–152. Chicago: IITRI.